Enhanced photoelectrocatalytic hydrogen production via Bi/BiVO$_4$ photoanode under visible light irradiation

Fang Li[a], Wei Zhao[a,b], Dennis Y.C. Leung[a,*]

[a] *Department of Mechanical Engineering, University of Hong Kong, Hong Kong, China*
[b] *School of Chemistry and Chemical Engineering, Huaiyin Normal University, Huaian, China*

ARTICLE INFO

ABSTRACT

Photoelectrocatalytic hydrogen production is a clean and sustainable way to combat energy crises and environmental issues. The performance of BiVO$_4$ which acts as a promising photoanode could be effectively enhanced by loading with Bi nanoparticles. In this study, a viable method to fabricate Bi/BiVO$_4$ electrode was proposed to enhance hydrogen production through a photoelectrocatalytic reaction. The results indicated that Bi nanoparticles loaded under optimal condition could obviously increase the photocurrent density of the BiVO$_4$ electrode from 0.9 mA cm^{-2} to 2.0 mA cm^{-2} under visible light illumination. Furthermore, the photoelectrochemical hydrogen production efficiency could have a 2.5-fold improvement with the addition of 20 ppm phenol. The possible mechanism of the enhanced performance and the function of phenol in the overall reaction was discussed.

1. Introduction

Global energy crisis and environmental pollution problems caused by fossil fuels had driven a lot of researches on clean and renewable energy. Photoelectrocatalytic water splitting was identified as a potential strategy to address the abovementioned problems due to the abundant water resource and solar light as well as the process is free of secondary pollution [1–4]. Thermodynamically, the decomposition of water is a difficult process, which required a high overpotential to achieve the overall water splitting. In this regard, ternary metal oxide materials with narrow bandgap, such as BiVO$_4$, Ag$_3$PO$_4$, CoTiO$_3$, Ag$_3$VO$_4$, MgFe$_2$O$_4$ and Bi$_2$WO$_6$, had attracted great interests for use in the photoelectrochemical reaction. Among these materials, the monoclinic BiVO$_4$ was considered as a promising photoanode owing to its suitable band position for photoelectrocatalytic water splitting [5–9].

Previous studies on the preparation of BiVO$_4$ mainly focused on the hydrothermal approaches to fabricate photocatalysts in powder forms [10]. The strong resistive force created between the catalyst and the conductive substrate in the photoelectrochemical process greatly reduced the efficiency of the reaction. Therefore, self-assembled materials grown directly on the substrate could enhance the binding force of photocatalysts with high stability, low transfer resistance and fast diffusion rate. A novel method of electrodeposition combined with thermal treatment was employed in this study to fabricate BiVO$_4$ photoelectrode that could achieve the abovementioned effects [5,11–13].

The performance of BiVO$_4$ photoelectrode could be significantly improved by modification of its composition and structure, such as impurity doping [13–16], crystal facet engineering [17,18] and heterojunction structure [19–22]. Among these, extensive research efforts had been devoted to the BiVO$_4$ loaded with a co-catalyst, which was considered as an effective route to enhance the photoelectrocatalytic performance of BiVO$_4$ electrode. For example, BiVO$_4$ could be coupled with oxygen evolution catalysts (OECs) materials (e.g. Co-Pi, FeOOH) to obtain a negative onset potential for water oxidation [23–25], or loaded with noble metal nanoparticles to build a plasmonic structure for enhancing visible light absorption [26–29]. Dong et al. reported in 2014 that bismuth (Bi), as a non-noble semi-metal, also possessed a direct plasmonic photocatalytic activity [30]. Subsequently, a large number of researches were carried out on the improvement of Bi/semiconductor heterostructure due to the low cost and excellent properties [12,31–34].

In the present study, a thin film of BiVO$_4$ electrode was prepared through electrodeposition method combined with thermal treatment. Fine Bi nanoparticles were further loaded onto the BiVO$_4$ by another electrodeposition process. The experimental parameters of the second electrodeposition process for loading Bi nanoparticles were optimized to avoid the destruction of the as-prepared BiVO$_4$ film under over-negative potential. The present electrodeposition preparation method of Bi/BiVO$_4$ electrode was compared with the photo-assisted reduction way as reported by Wang et al. [12] from the aspects of nanostructure

---

and composition. The enhancement of Bi/BiVO$_4$ electrode was ascribed to the heterojunction structure between the metal and the semiconductor, retarding the recombination of photo-induced charge pairs as well as increasing the transfer rate of charge carriers. The performance of the Bi/BiVO$_4$ electrode was measured with the reaction of photoelectrocatalytic hydrogen production, and surprisingly found that the efficiency of hydrogen production could be significantly improved by the addition of phenol, a common pollutant existed in wastewater. This work might give a new insight for changing the role of expensive platinum electrode in photoelectrocatalytic hydrogen production.

2. Experimental section

2.1. Material

In-doped SnO$_2$ coated glass (ITO, H-NXC Technology Co., Ltd., 20 mm x 10 mm x 1.1 mm, 6 Ω/sq), bismuth nitrate pentahydrate (Bi(NO$_3$)$_3$·5H$_2$O, ≥ 99.99%, metals basis, Aladdin, China), potassium perchlorate (KClO$_4$, AR, Aladdin, China), vanadyl acetylacetonate (VO(acac)$_2$, 98%, Aladdin, China), ethylene glycol (AR, 99.5%, Sigma-Aldrich, USA), dimethyl sulfoxide (DMSO, AR, Aladdin, China), sodium hydroxide (NaOH, ACS, Honeywell, USA), sodium sulfate (Na$_2$SO$_4$, ACS, Sigma-Aldrich, USA), phenol (AR, Aladdin, China).

2.2. Preparation of Bi/BiVO$_4$

Bi/BiVO$_4$ photoelectrode was fabricated through two steps. First, the BiVO$_4$ was prepared by electrodeposition combined with thermal treatment method, which was similar to the procedures of Kim et al. [11]. Generally, a layer of Bi nanoparticles was deposited onto the surface of an ITO glass equipped with a typical three-electrode system in an ethylene glycol solution (50 mL) containing 0.485 g Bi(NO$_3$)$_3$·5H$_2$O and 0.693 g KClO$_4$. The ITO, platinum (Pt) sheet and saturated calomel electrode (SCE) served as working electrode, counter electrode and reference electrode, respectively. The working electrode with ~1 cm^2 immersed area was conducted with a constant potential of -1.5 V for 10 s, followed by an interval time of 10 s rest for replenishment of Bi^{3+} in the vicinity of the electrode, thereby 20 s were considered as one cycle for the Bi deposition. The amount of Bi could be controlled by repeating the cycles. After electrodeposition, the as-prepared Bi electrode was covered by 100 μL 50 mM VO(acac)$_2$ solution in DMSO as a precursor of vanadium, then carefully transferred to a muffle furnace for heat treatment at 450 °C for 3 h. In the thermal process, Bi reacted with VO^{2+} to synthesize BiVO$_4$, residual reactant could be removed by immersing the electrode in 1 M NaOH solution until the surface of the electrode changed to yellow. Then, the electrode was rinsed with deionized water and dried at 60 °C.

The loading of Bi nanoparticles onto the BiVO$_4$ electrode followed the same electrodeposition procedure as described above. The applied potential and deposition time were lowered to −1.0 V and 2 s to protect the as-obtained BiVO$_4$ film. For comparison, photo-assisted reduction method was also employed to fabricate Bi/BiVO$_4$ in 10 mM Bi(NO$_3$)$_3$·5H$_2$O mixture solution of 1:1 (volume ratio) ethylene glycol and water under illumination of 60 min [12]. The sample electrodes were named with a suffix of loading method (that is, ED and PR for electrodeposition and photo-assisted reduction method).

2.3. Characterization

The morphology of the as-prepared electrode samples was observed by a field emission scanning electron microscope (FESEM, Hitachi S-4800, Japan). The crystal compositions of samples were characterized by X-ray diffraction (XRD, PANalytical model X'Pert PRO diffractometer, Holland) with Cu Kα radiation, 2θ ranged from 20° to 80° with a speed of 20°/min. The surface electronic states of samples were analyzed by X-ray photoelectron spectroscopy (XPS, Perkin-Elmer PHI

5000, USA) with Al Kα (1486.6 eV) radiation, the binding energy values were calibrated using C1 s = 284.65 eV as a reference. The light absorption ability of samples was measured by ultraviolet-visible diffuse reflectance spectra (UV–vis DRS, Shimadzu UV 2600, Japan) of a spectrophotometer with BaSO$_4$ powder as the reference. Photoelectrochemical measurements were carried out by an electrochemical workstation (CH Instruments Inc CHI-660E, China). Hydrogen was detected by gas chromatography (GC, Purui GC-7800, China). The concentration of phenol and the reaction products were analysed by high performance liquid chromatography (HPLC, Shimadzu LC-20AD, Japan). Density functional theory (DFT) simulations were performed with the generalized gradient approximation (GGA) with the Perdew-Burke-Ernzerhof (PBE) method to calculate the work function in the CASTEP code.

2.4. Photoelectrochemical measurement and activity test

Photocurrent tests were measured with the three-electrode system in an electrolytic cell with a flat quartz window. The sample working electrode was applied with a bias potential of + 0.5 V in a 0.2 M Na$_2$SO$_4$ solution under visible light irradiation of a 300 W Xenon lamp (100 mW/cm^2) with a filter (> 420 nm). Pt sheet and SCE acted as counter electrode and reference electrode, respectively. The photoelectrocatalytic hydrogen production experiment was conducted in an airtight cell with the three-electrode system under the same condition as the photoelectrochemical test.

3. Result and discussion

3.1. Morphology and composition analysis

The crystalline phase and composition of the sample electrodes synthesized in each step were characterized by XRD pattern as shown in Fig. 1. After the first Bi electrodeposition step, the characteristic diffraction peaks could be observed matching the phase of Bi metal (JCPDS NO.: 44-1246). Thereafter, the peaks of Bi metal disappeared in the process of thermal treatment for the conversion of Bi to BiVO$_4$, the characteristic peak at 28.9 ° could be assigned to the crystalline phase of BiVO$_4$ (-121) (JCPDS NO.: 14-0688), which indicated that the conversion of BiVO$_4$ was completed without trace of Bi metal left. For comparing the electrodeposition method with the photo-assisted reduction method of loading Bi onto the surface of BiVO$_4$, these two kinds of as-prepared Bi/BiVO$_4$ electrode were characterized by XRD pattern. The results showed that Bi/BiVO$_4$ was successfully fabricated, because all the characteristic peaks could be matched to the crystalline phase of Bi
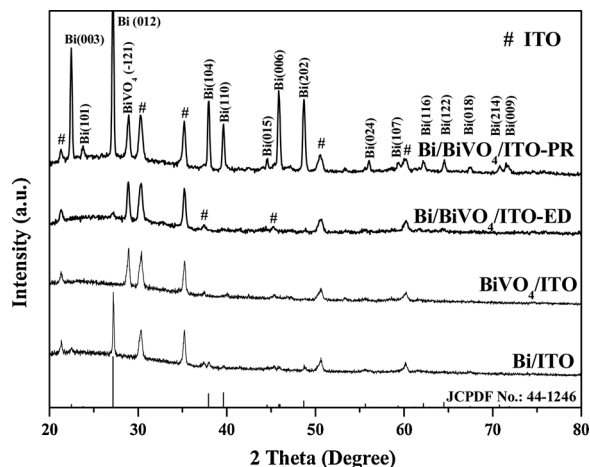

Fig. 1. XRD patterns of pre-loaded Bi metal, BiVO$_4$, Bi/BiVO$_4$-ED and Bi/BiVO$_4$-PR deposited on ITO glass.
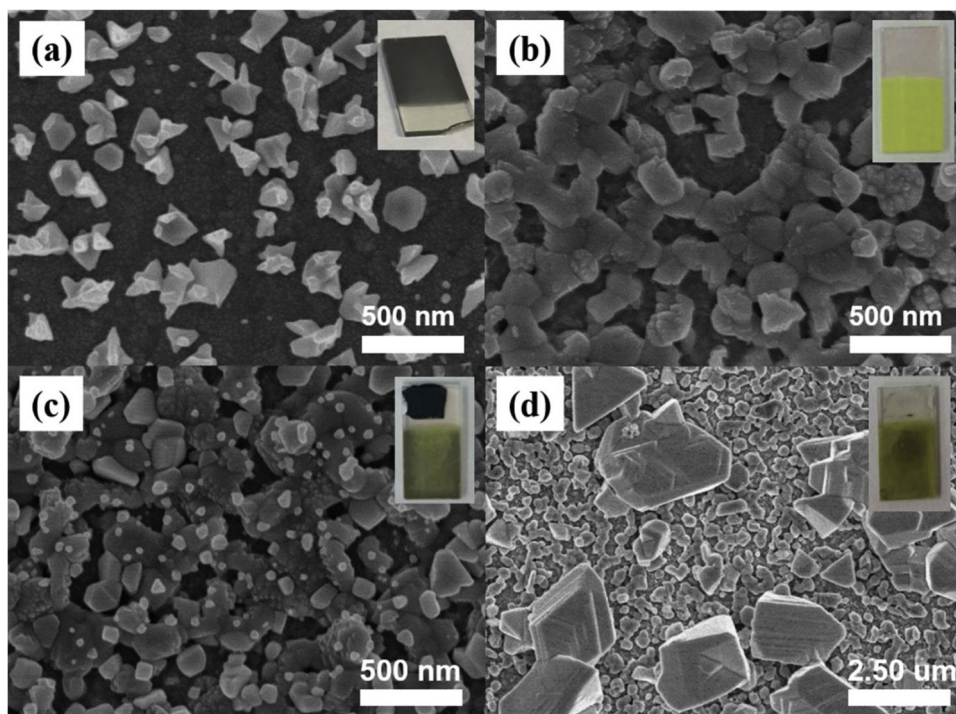
Fig. 2. SEM images of (a) pre-loaded Bi metal; (b) bare $BiVO_4$; (c) Bi/$BiVO_4$-ED; (d) Bi/$BiVO_4$-PR. (ED: Electrodeposition; PR: Photo-assisted reduction).

and $BiVO_4$ as mentioned above. However, the Bi/$BiVO_4$ synthesized through photo-assisted reduction method (Bi/$BiVO_4$-PR) displayed much stronger peak intensity of loaded Bi metal than that of Bi/$BiVO_4$ synthesized by electrodeposition method (Bi/$BiVO_4$-ED), which might be explained by the large particle size of the loaded Bi metal associated with the photo-assisted reduction method.

The morphology and structure of the as-prepared electrodes are shown in the Fig. 2. Bi nanoparticles of a size ranged from 50 to 200 nm were deposited on the conductive substrates by the electrochemical method (Fig. 2a), subsequently reacted with the vanadium precursor to obtain a porous $BiVO_4$ nanostructure (Fig. 2b). Compared to the bare $BiVO_4$, it is obvious that the Bi metal, which had been confirmed by the XRD analysis, was highly dispersed on $BiVO_4$ for both electrodeposition and photoreduction methods. However, the loaded Bi particle size was much different from each other. The Bi particles size of Bi/BiVO-PR shown in Fig. 2d was in line with that of Wang et al. [13]. This result suggested that the electrodeposition method could fabricate much smaller Bi nanoparticles (20~100 nm) than that of the photo-assisted reduction route, which should attribute to the pulsed electrochemical deposition process that increase the opportunity of crystalline nucleation instead of growing to a large particle.

Further evidence of Bi loaded onto the surface of $BiVO_4$ was presented by the XPS results as shown in Fig. 3. The peak positions of Bi 4f were calibrated against C 1s with 284.5 eV binding energy. Fig. 3a showed the XPS survey spectrums of the as-prepared $BiVO_4$ and Bi/$BiVO_4$-ED electrodes, the results revealed that the chemical composition of the sample electrodes contained Bi, V, O, and C. Fig. 3b showed the high-resolution XPS spectrum of Bi 4f in both the $BiVO_4$ and Bi/$BiVO_4$ electrodes. For the bare $BiVO_4$, the peaks at 164.1 eV and 158.8 eV attached to Bi 4f7/2 and Bi 4f5/2, respectively, which should be ascribed to Bi^{3+} in $BiVO_4$. This result also proved the complete conversion of Bi to $BiVO_4$ through the thermal treatment. While in the XPS spectrum of Bi/$BiVO_4$, the two weak peaks, appeared at the binding energy of 161.8 eV and 156.5 eV after electrodeposition process, were ascribed to the formation of Bi metal with Bi^0 in the Bi/$BiVO_4$ electrode [35]. According to the area of the characteristic peak of Bi^0 (refer to metallic Bi) and Bi^{3+} (refer to $BiVO_4$) in Fig. 3b, the

loading amount of Bi nanoparticles in Bi/$BiVO_4$-ED sample was about 8.4 wt%. Compared with the bare $BiVO_4$, the binding energy of the two Bi^{3+} 4f peaks for Bi/$BiVO_4$ showed slightly negative shift (less than 0.2 eV). Besides, the same shift tendency could also be observed in the high-resolution XPS spectrum of V 2p region and O 1s region for Bi/$BiVO_4$. The negative shift proved that the feasibility of the interfacial electron transfer between the metal Bi and semiconductor $BiVO_4$ in the Bi/$BiVO_4$ sample.

3.2. Optical and photoelectrochemical properties

The UV–vis DRS of the as-prepared sample electrodes were shown in Fig. 4a. The absorption at less than 510 nm for all the sample electrodes could be attributed to the intrinsic absorption band of $BiVO_4$. Compared to the bare $BiVO_4$, Bi/$BiVO_4$-ED and Bi/$BiVO_4$-PR exhibited an obvious improvement in light absorption larger than 510 nm, which was explained by the dark color of the composited samples due to the metallic Bi nanoparticles loading [36]. However, a weak surface plasmon resonance (SPR) absorption band of Bi/$BiVO_4$ sample was observed at around 560 nm owing to the SPR property of Bi metal, the results were in accordance with the results of previous studies [36–38]. The energy bandgap of each sample was determined by using the transformation of Kubelka-Munk function and presented in Fig. 4c–e. The result revealed that loading of Bi metal would slightly narrow down the bandgap value of $BiVO_4$, and the smaller particle size of metallic Bi tended to exhibit a more obvious effect on the composite material. In the photocurrent tests of the sample electrodes shown in Fig. 4b, the bare $BiVO_4$ gave an anodic photocurrent intensity of 0.85 mA cm^{-2} under visible light irradiation. Compared with bare $BiVO_4$, both the Bi/$BiVO_4$-ED and -PR electrodes obtained an extensive rise in photocurrent density. The smaller Bi nanoparticles with larger contact area could accelerate the transfer rate of charge carriers between Bi metal and $BiVO_4$, as well as provide more active sites during the reaction, thus the Bi/$BiVO_4$-ED electrode showed a much higher photocurrent density than that of Bi/$BiVO_4$-PR electrode. This result revealed that the electrodeposition method was an excellent route to fabricate the Bi/$BiVO_4$ heterostructure with small particle size and high dispersion of Bi semi-metal
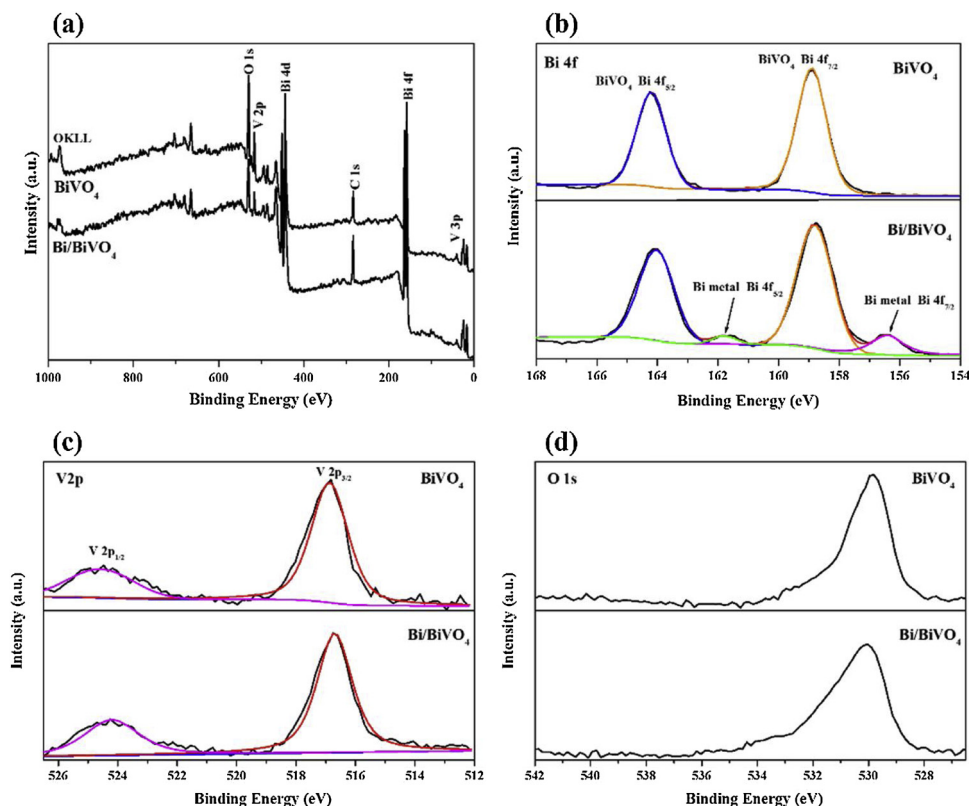
Fig. 3. (a) Full XPS spectrum and high-resolution XPS spectrum of (b) Bi 4f; (c) V 2p and (d) O 1s for the as-prepared $BiVO_4$ and $Bi/BiVO_4$ electrodes.

nanoparticles than the photoreduction method.

The amount of Bi nanoparticles loaded onto the surface of $BiVO_4$ was optimized by controlling the deposition time (that is, 10 s, 30 s and 50 s) as shown in Fig. 5a–d. It was found that the particle size of Bi metal loaded kept growing up with increasing the deposition time and even covered the whole surface of $BiVO_4$ forming a shielding effect. Thus, extensive deposition time would weaken the superiority of Bi/$BiVO_4$-ED electrode, as indicated in Fig. 5e. Jing et al. [31] also reported that overloading Bi nanoparticles would serve as mediators to raise the recombination rate of photo-induced charge pairs and cause a decrease in activity performance. The Bi/$BiVO_4$-ED-30 s showed the optimum photocurrent density among the three deposition times tested.

3.3. Theoretical calculation

According to the XRD results, the monoclinic $BiVO_4$ structure was chosen for the theoretical calculation. DFT simulation was carried out with the GGA-PBE method, the calculated energy band structure and
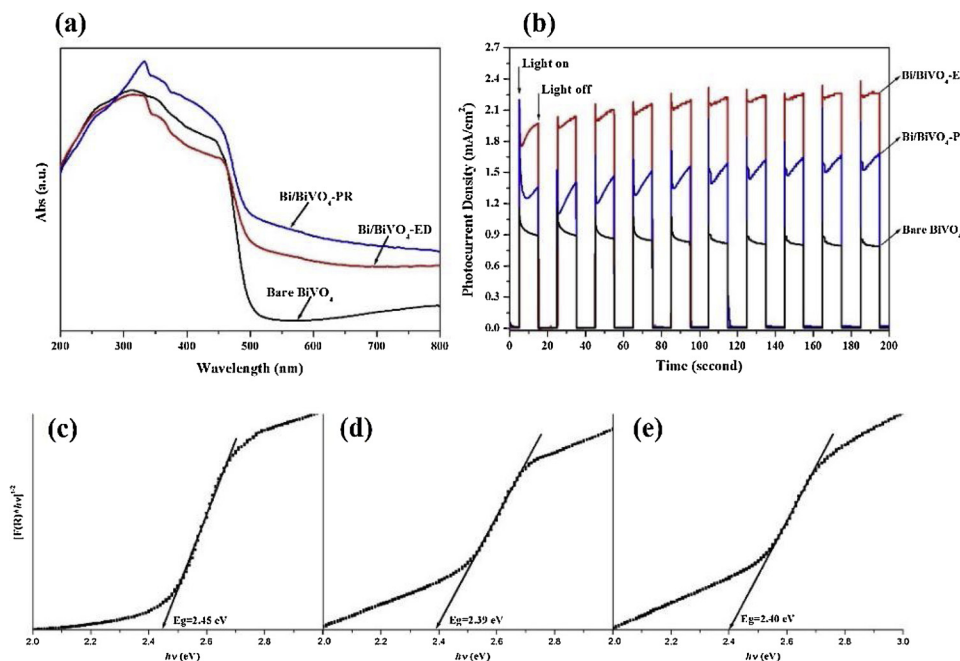

Fig. 4. (a) UV–vis diffuse reflectance spectrums of $BiVO_4$ and $Bi/BiVO_4$ electrodes; (b) Transient photocurrent density of the sample electrodes applied with $+0.5$ V bias potential in a 0.2 M Na_2SO_4 solution under visible light (> 420 nm) irradiation; (c) Kubelka–Munk plots of $BiVO_4$ electrode, (d) Bi/$BiVO_4$-ED electrode and (e) Bi/$BiVO_4$-PR electrode.
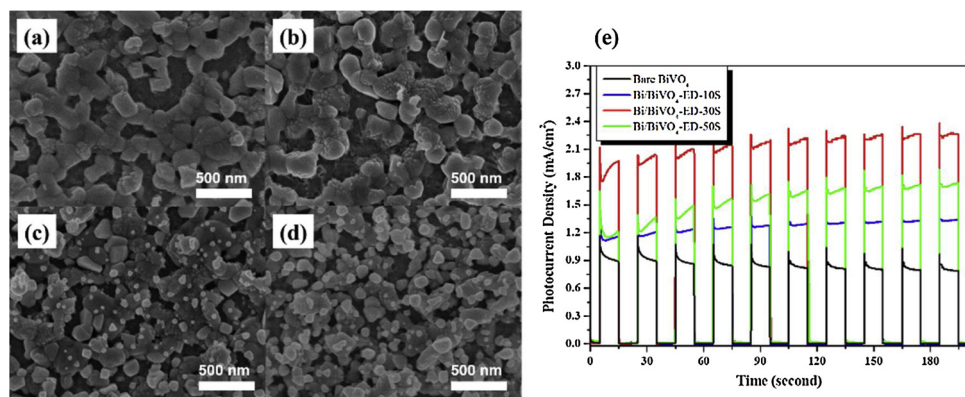
Fig. 5. SEM images of (a) bare BiVO$_4$; (b) Bi/BiVO$_4$-ED-10 s; (c) Bi/BiVO$_4$-ED-30 s; (d) Bi/BiVO$_4$-ED-50 s (time refer to duration time in the process of Bi electrodeposition); (e) Transient photocurrent density of different sample electrodes applied with +0.5 V bias potential in a 0.2 M Na$_2$SO$_4$ solution under visible light (> 420 nm) irradiation.
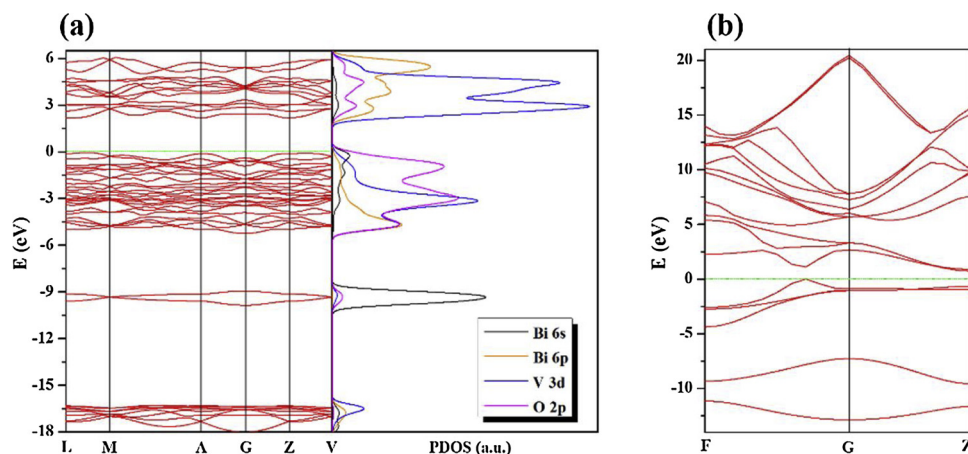

Fig. 6. (a) Calculated energy band structure and corresponding density of state of the monoclinic BiVO$_4$; (b) Calculated energy band structure of the Bi bulk. Fermi level was set to be zero, shown as the green dash line (For interpretation of the references to colour in this figure legend, the reader is referred to the web version of this article).
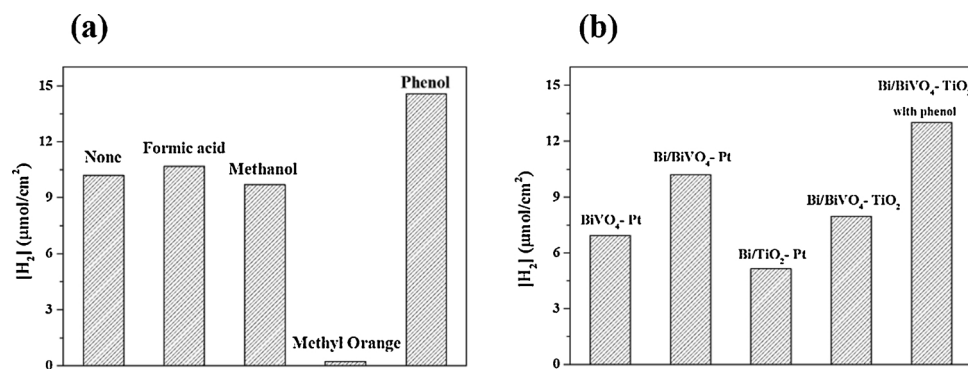

Fig. 7. (a) Effect of additives on the photoelectrocatalytic hydrogen production with Bi/BiVO$_4$ as the photoanode under visible light irradiation (Irradiation area of photoanode was 1 cm × 1 cm); (b) Effect of different materials on photoelectrocatalytic hydrogen production activities of sample photoelectrode (that is, photoanode - cathode as indicated for each bar).

DOS results of the geometry optimized BiVO$_4$ (001) was shown in Fig. 6a, while the stability of BiVO$_4$(001) surface had been discussed and confirmed by previous reports [39,40]. The optimized crystal structures of BiVO$_4$ and Bi bulk were shown in Fig S3. The simulated band structure of BiVO$_4$ indicated that a minimum indirect energy band gap of 2.23 eV occurred between the *k*-points direction of L and M. Besides, two more direct energy band gaps could be observed along the A point and Z point, which mainly contributed to the visible-light-response of BiVO$_4$ [40,41]. Compared with the experimental value of bare BiVO$_4$ as shown in Fig. 4c, the simulated energy band gap was 0.22 eV smaller, which should be ascribed to the typical restriction of the DFT calculation for semiconductors [19]. The atomic orbitals of Bi, V and O had been simulated and correlated to the energy band structure in Fig. 6a to explore the band edges and hybridization states of BiVO$_4$. The valance band maximum (VBM) of BiVO$_4$ was occupied by O 2p orbitals, while hybridized with V 3d and Bi 6p orbitals forming V−O and Bi−O bonding states, respectively. However, the conduction band minimum (CBM) was significantly dominated by 3d orbitals of V atoms with partial contribution of Bi 6p and O 2p orbitals [39,42]. In comparison with the bare BiVO$_4$, the bandgap value of the Bi/BiVO$_4$ showed a slight drop from 2.45 eV to 2.39 eV in Fig. 4, indicating that the loading of Bi nanoparticles had a weak impact upon changing the bandgap structure of the BiVO$_4$ [43,44]. On the other hand, the excited photoelectrons from the metallic Bi nanoparticles formed excess charges localized on the V atoms of BiVO$_4$ when their surfaces were in contact [45]. Therefore, the enhancement performance of the Bi/BiVO$_4$ could be explained by the increased charge transport rate as well as the SPR effect of Bi nanoparticles.

3.4. Photoelectrocatalytic hydrogen production activities

The photoelectrocatalytic (PEC) activities of the sample electrodes, measured through the hydrogen production reaction under different experimental conditions are shown in Fig. 7. In the process of PEC
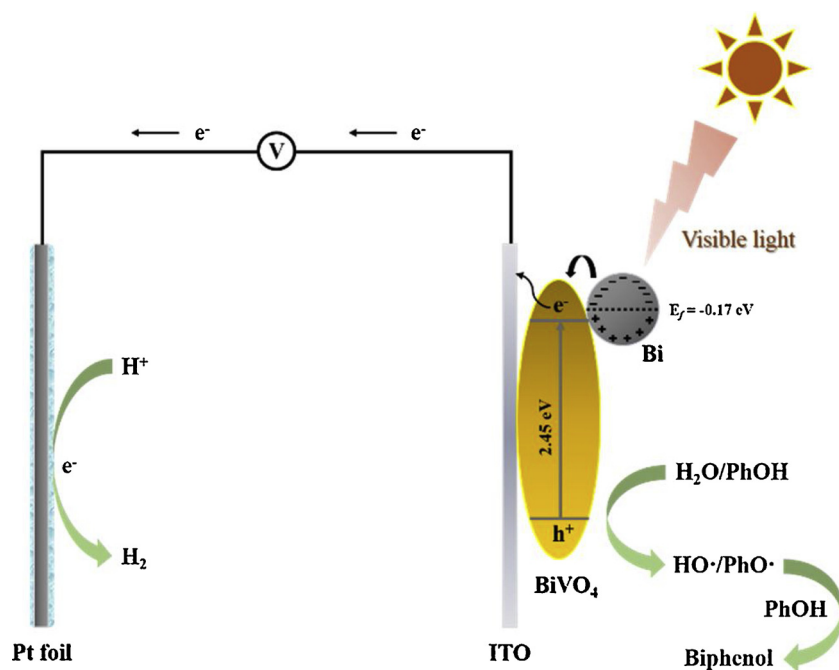
Fig. 8. Illustration of the mechanism for photoelectrocatalytic hydrogen production with Bi/BiVO$_4$.

hydrogen production with n-type semiconductor, photoelectrons, as the majority charge carriers, were generated from induced photoanode, which were then transferred to the counter electrode through the external circuit to form the hydrogen. Diagrammatic sketch of the reaction process was displayed in Fig. 8. In the system, the capability of the photoanode would be affected from the recombination yield of charge carriers, kinetics rate of reaction and response range of the photocatalyst all of which paid major roles for the overall activity of reaction [1]. BiVO$_4$ was considered as a potential photoanode for the PEC hydrogen production owing to its narrow bandgap and suitable energy band structure, the loading of Bi nanoparticles could efficiently inhibit recombination of the photo-induced charge carriers to improve the photocatalytic activity. In Fig. 7a, low concentration (that is, 10 ppm) of additives (that is, phenol and formic acid) was added to the reaction system to investigate their influence on the hydrogen production efficiency with the Bi/BiVO$_4$ as the photoanode. The results revealed that the addition of formic acid or phenol would enhance the hydrogen production rate owing to the fact that the O−H bonds in formic acid and phenol were weaker than that of H$_2$O, thus easier to form the dissociated hydrogen ion (H$^+$). However, the enhancement of hydrogen production was greater for phenol than for formic acid, as shown in

Fig. 7a, which might be caused by the phenoxyl radicals, as discussed in the subsequent paragraph. On the contrary, the hydrogen production rate slightly decreased with addition of methanol due to the strong O−H bond in methanol. Moreover, the hydrogen production rate was seriously affected by adding methyl orange, because the light absorption between 400~500 nm of Bi/BiVO$_4$ had been impeded by the presence of methyl orange. Alternatively, TiO$_2$ nanotube arrays was chosen as a photo-responsive substrate with loading of Bi nanoparticles (Bi/TiO$_2$) for comparative investigation of the Bi/BiVO$_4$, which revealed a decreased hydrogen production rate, as shown in Fig. 7b. Tong et al. [20] reported that a heterostructured TiO$_2$/BiVO$_4$/Co-Pi photoanode performed ~8.0 μmol cm^{-2} h^{-1} hydrogen production rate, which was also lower than that of Bi/BiVO$_4$ in the present study (that is, 10.6 μmol cm^{-2} h^{-1}). The results indicated that BiVO$_4$ is a superior photoanode to serve as photo-responsive substrate rather than TiO$_2$ for further modification with Bi. Besides, we tried to replace the expensive Pt electrode by TiO$_2$-based material for hydrogen production but a relatively reduced activity was obtained. However, the hydrogen production rate could be significantly improved by the addition of phenol even using TiO$_2$ as cathode as shown in Fig. 7b, which provided an economic strategy for photoelectrocatalytic hydrogen production.
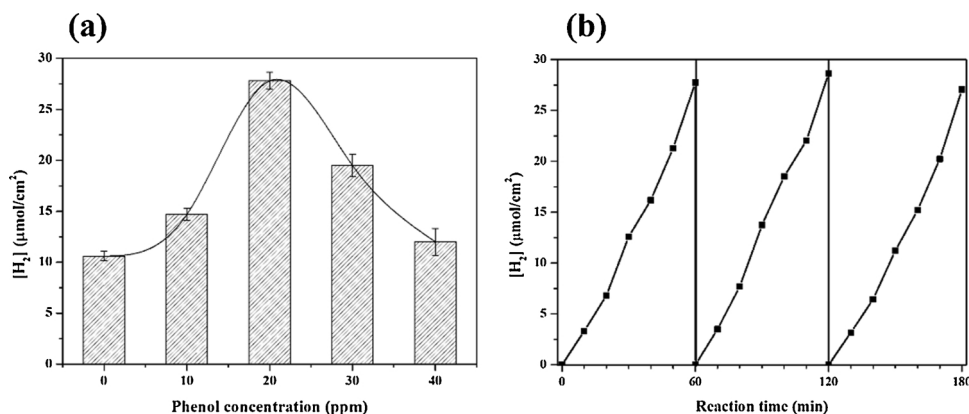

Fig. 9. Effect of phenol concentrations on the photoelectrocatalytic hydrogen production rate; (b) stability test of Bi/BiVO$_4$ photoelectrode for photoelectrocatalytic hydrogen production reaction under visible light irradiation.

$$H_2O \longrightarrow \cdot OH + H^+ + e^- \qquad (1)$$

$$\text{(phenol)} \longrightarrow \text{(phenoxyl radical)} + H^+ + e^- \qquad (2)$$

$$\text{(phenol)} + \cdot OH \longrightarrow \text{(phenoxyl radical)} + H_2O \qquad (3)$$

$$\text{(phenoxyl radical)} + \text{(phenoxyl radical)} \longrightarrow \text{Biphenol products} \qquad (4)$$
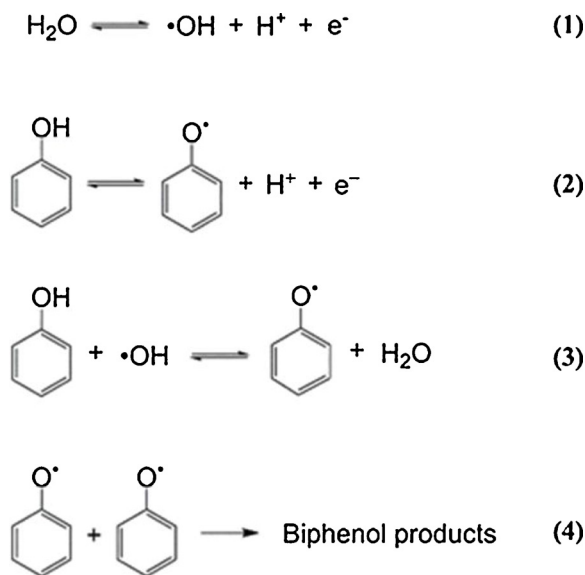
Fig. 10. Proposed mechanism of the reaction path.

The influence of phenol concentration on hydrogen production rate was further investigated in the system consisting of Bi/BiVO$_4$- Pt as presented in Fig. 9a. The hydrogen production rate rose from 10.6 μmol cm^{-2} h^{-1} to 27.8 μmol cm^{-2} h^{-1} with increasing the concentration of phenol from 0 to 20 ppm, thereafter the hydrogen production rate decreased with further increasing phenol concentration.

According to this result, the mechanism of the reaction path was proposed as in Fig. 10. First, hydroxyl radical and phenoxyl radical were generated at the surface of the photoanode during Step 1 and Step 2. Meanwhile, abundant H$^+$ and electrons were generated and transferred to the surface of cathode for the hydrogen production. On the other hand, the phenoxyl radical was more stable than the hydroxyl radicals due to the delocalization effect of unpaired electron around the benzene ring, therefore, existence of phenol could accelerate the consumption of the hydroxyl radicals (Step 3) [46,47], whereas increased the reaction rate in Step 1, which was the rate-determining step of the hydrogen production reaction. However, when the concentration of phenol kept increasing, the dissociation of phenol (Step 2) became more competitive than that of H$_2$O (Step 1), meaning that the generation rate of the hydroxyl radicals would be slowed down. As well, the H atom abstraction process of the hydroxyl radicals from phenol could be suppressed. In order to explore the final product of phenol, UV–vis DRS and high performance liquid chromatography (HPLC) were employed to analyze the liquid samples, as shown in the supplementary information. The DRS spectrum showed that the intensity of characteristic peak for phenol at ~270 nm had not decrease after 2 -h reaction, and another characteristic peak (at ~245 nm) appeared with a wide absorption range. The HPLC analysis illustrated that the concentration of phenol (at retention time of ~4.0 min) had only reduced by ~41% after reaction, but an obvious peak occurred at ~2.7 min, which belonged to the dimeric intermediate of phenol (that is, biphenol) synthesized from phenoxyl radicals (Step 4) [46,48,49]. The stability of the as-prepared Bi/BiVO$_4$ electrode was measured in the photoelectrocatalytic hydrogen production reaction. As shown in Fig. 9b, the reaction time extended to 180 min running three consecutive tests, and the hydrogen production efficiency had no obvious reduction, which implied great repeatability of the Bi/BiVO$_4$ electrode for photoelectrocatalytic reaction.

4. Conclusions

In summary, semi-metal Bi nanoparticles loaded on BiVO$_4$ electrode

was fabricated through a two-step electrodeposition process, the heterostructure of Bi/BiVO$_4$ exhibited an enhanced optical and catalytic performance. The photocurrent density of Bi/BiVO$_4$-ED sample electrode could reach 2.1 mA cm^{-2} with a +0.5 V*vs* $_{SEC}$ bias potential under visible light irradiation. The enhancement of Bi/BiVO$_4$ electrode should be attributed to the reduced recombination rate of photo-induced charge pairs as well as more effective contact between Bi nanoparticles and BiVO$_4$. The photoelectrochemical hydrogen production was studied with Bi/BiVO$_4$ as photoanode, the activity results indicated that the addition of phenol significantly improved the hydrogen production rate. The current work provided a new strategy to deal with the study of solar energy conversion in the future.

Declaration of Competing Interest

Nothing declared.

Appendix A. Supplementary data

Supplementary material related to this article can be found, in the online version, at doi:https://doi.org/10.1016/j.apcatb.2019.117954.

References

[1] H.L. Tan, R. Amal, Y.H. Ng, Alternative strategies in improving the photocatalytic and photoelectrochemical activities of visible light-driven BiVO$_4$: a review, J. Mater. Chem. A 5 (2017) 16498–16521.

[2] X. Li, J. Yu, J. Low, Y. Fang, J. Xiao, X. Chen, Engineering heterogeneous semiconductors for solar water splitting, J. Mater. Chem. A 3 (2015) 2485–2534.

[3] T. Hisatomi, J. Kubota, K. Domen, Recent advances in semiconductors for photocatalytic and photoelectrochemical water splitting, Chem. Soc. Rev. 43 (2014) 7520–7535.

[4] J. Gan, X. Lu, Y. Tong, Towards highly efficient photoanodes: boosting sunlight-driven semiconductor nanomaterials for water oxidation, Nanoscale 6 (2014) 7142–7164.

[5] D. Kang, Y. Park, J.C. Hill, K.S. Choi, Preparation of Bi-based ternary oxide photoanodes BiVO$_4$, Bi$_2$WO$_6$, and Bi$_2$Mo$_3$O$_{12}$ using dendritic Bi metal electrodes, J. Phys. Chem. Lett. 5 (2014) 2994–2999.

[6] S. Wang, P. Chen, Y. Bai, J.H. Yun, G. Liu, L. Wang, New BiVO$_4$ dual photoanodes with enriched oxygen vacancies for efficient solar-driven water splitting, Adv. Mater. 30 (2018) e1800486.

[7] D.K. Lee, K.-S. Choi, Enhancing long-term photostability of BiVO$_4$ photoanodes for solar water splitting by tuning electrolyte composition, Nat. Energy 3 (2017) 53–60.

[8] Z.F. Huang, L. Pan, J.J. Zou, X. Zhang, L. Wang, Nanostructured bismuth vanadate-based materials for solar-energy-driven water oxidation: a review on recent progress, Nanoscale 6 (2014) 14044–14063.

[9] M.N. Shaddad, P. Arunachalam, J. Labis, M. Hezam, A.M. Al-Mayouf, Fabrication of robust nanostructured (Zr) BiVO$_4$/nickel hexacyanoferrate core/shell photoanodes for solar water splitting, Appl. Catal. B (2018).

[10] F.Q. Zhou, J.C. Fan, Q.J. Xu, Y.L. Min, BiVO$_4$ nanowires decorated with CdS nanoparticles as Z-scheme photocatalyst with enhanced H$_2$ generation, Appl. Catal. B 201 (2017) 77–83.

[11] H.R. Kim, G. Kim, S.-I. In, Y. Park, Optimization of porous BiVO$_4$photoanode from electrodeposited Bi electrode: structural factors affecting photoelectrochemical performance, Electrochim. Acta 189 (2016) 252–258.

[12] Q. Wang, J. He, Y. Shi, S. Zhang, T. Niu, H. She, Y. Bi, Designing non-noble/ semiconductor Bi/BiVO$_4$ photoelectrode for the enhanced photoelectrochemical performance, Chem. Eng. J. 326 (2017) 411–418.

[13] S. Xie, T. Zhai, Y. Zhu, W. Li, R. Qiu, Y. Tong, X. Lu, NiO decorated Mo:BiVO$_4$ photoanode with enhanced visible-light photoelectrochemical activity, Int. J. Hydrogen Energy 39 (2014) 4820–4827.

[14] O.K. Okoth, K. Yan, J. Zhang, Mo-doped BiVO$_4$ and graphene nanocomposites with enhanced photoelectrochemical performance for aptasensing of streptomycin, Carbon 120 (2017) 194–202.

[15] A.J.E. Rettie, W.D. Chemelewski, J. Lindemuth, J.S. McCloy, L.G. Marshall, J. Zhou, D. Emin, C.B. Mullins, Anisotropic small-polaron hopping in W: BiVO$_4$ single crystals, Appl. Phys. Lett. 106 (2015) 022106.

[16] B.J. Trześniewski, W.A. Smith, Photocharged BiVO4 photoanodes for improved solar water splitting, J. Mater. Chem. A 4 (2016) 2919–2926.

[17] R. Li, H. Han, F. Zhang, D. Wang, C. Li, Highly efficient photocatalysts constructed

by rational assembly of dual-cocatalysts separately on different facets of BiVO₄, Energy Environ. Sci. 7 (2014) 1369–1376.

[18] S.M. Thalluri, S. Hernández, S. Bensaid, G. Saracco, N. Russo, Green-synthesized W- and Mo-doped BiVO₄ oriented along the {0 4 0} facet with enhanced activity for the sun-driven water oxidation, Appl. Catal. B 180 (2016) 630–636.

[19] S.N.F.M. Nasir, H. Ullah, M. Ebadi, A.A. Tahir, J.S. Sagu, M.A. Mat Teridi, New insights into Se/BiVO₄ heterostructure for photoelectrochemical water splitting: a combined experimental and DFT study, J. Phys. Chem. C 121 (2017) 6218–6228.

[20] R. Tong, X. Wang, X. Zhou, Q. Liu, H. Wang, X. Peng, X. Liu, Z. Zhang, H. Wang, P.D. Lund, Cobalt-phosphate modified TiO₂/BiVO₄ nanoarrays photoanode for efficient water splitting, Int. J. Hydrogen Energy 42 (2017) 5496–5504.

[21] X. Chang, T. Wang, P. Zhang, J. Zhang, A. Li, J. Gong, Enhanced surface reaction kinetics and charge separation of p–n heterojunction Co₃O₄/BiVO₄ photoanodes, J. Am. Chem. Soc. 137 (2015) 8356–8359.

[22] Y. Liu, B.R. Wygant, K. Kawashima, O. Mabayoje, T.E. Hong, S.-G. Lee, J. Lin, J.-H. Kim, K. Yubuta, W. Li, Facet effect on the photoelectrochemical performance of a WO₃/BiVO₄ heterojunction photoanode, Appl. Catal. B 245 (2019) 227–239.

[23] A. Jia, M. Kan, J. Jia, Y. Zhao, Photodeposited FeOOH vs electrodeposited Co-Pi to enhance nanoporous BiVO₄ for photoelectrochemical water splitting, J. Semicond. 38 (2017) 053004.

[24] B. Peng, M. Xia, C. Li, C. Yue, P. Diao, Network structured CuWO₄/BiVO₄/Co-Pi nanocomposite for solar water splitting, Catalysts 8 (2018) 663.

[25] L. Xia, J. Bai, J. Li, Q. Zeng, L. Li, B. Zhou, High-performance BiVO₄ photoanodes cocatalyzed with an ultrathin α-Fe₂O₃ layer for photoelectrochemical application, Appl. Catal. B 204 (2017) 127–133.

[26] Z. Wei, D. Benlin, Z. Fengxia, T. Xinyue, X. Jiming, Z. Lili, L. Shiyin, D.Y.C. Leung, C. Sun, A novel 3D plasmonic p-n heterojunction photocatalyst: Ag nanoparticles on flower-like p-Ag₂S/n-BiVO₄ and its excellent photocatalytic reduction and oxidation activities, Appl. Catal. B 229 (2018) 171–180.

[27] Y. Liu, J. Kong, J. Yuan, W. Zhao, X. Zhu, C. Sun, J. Xie, Enhanced photocatalytic activity over flower-like sphere Ag/Ag₂CO₃/BiVO₄ plasmonic heterojunction photocatalyst for tetracycline degradation, Chem. Eng. J. 331 (2018) 242–254.

[28] Z. Wei, F. Yue, Z. Jin, Z. Fengxia, S. Zhen-Huan, D. Benlin, D.Y.C. Leung, Z. Lili, X. Jiming, A novel Ag/p-AgBr/n-BiVO₄ plasmonic heterojunction photocatalyst: study on the excellent photocatalytic performance and photocatalytic mechanism, ACS Appl. Energy Mater. (2018).

[29] B. Chen, Z. Zhang, M. Baek, S. Kim, W. Kim, K. Yong, An antenna/spacer/reflector based Au/BiVO₄/WO₃/Au nanopatterned photoanode for plasmon-enhanced photoelectrochemical water splitting, Appl. Catal. B (2018).

[30] F. Dong, T. Xiong, Y. Sun, Z. Zhao, Y. Zhou, X. Feng, Z. Wu, A semimetal bismuth element as a direct plasmonic photocatalyst, Chem. Commun. 50 (2014) 10386–10389.

[31] Q. Jing, X. Feng, X. Zhao, Z. Duan, J. Pan, L. Chen, Y.-N. Liu, Bi/BiVO₄ chain-like hollow microstructures: synthesis, characterization and application as visible-light-active photocatalysts, Acs Appl. Nano Mater. (2018) 2653–2661.

[32] Z. Zhao, W. Zhang, X. Lv, Y. Sun, F. Dong, Y. Zhang, Noble metal-free Bi nanoparticles supported on TiO₂ with plasmon-enhanced visible light photocatalytic air purification, Environ. Sci. Nano 3 (2016) 1306–1317.

[33] X. Li, W. Zhang, J. Li, G. Jiang, Y. Zhou, S. Lee, F. Dong, Transformation pathway and toxic intermediates inhibition of photocatalytic NO removal on designed Bi

[34] metal@defective Bi₂O₂SiO₃, Appl. Catal. B 241 (2019) 187–195.

[34] Z. Wang, S. Yan, Y. Sun, T. Xiong, F. Dong, W. Zhang, Bi metal sphere/graphene oxide nanohybrids with enhanced direct plasmonic photocatalysis, Appl. Catal. B 214 (2017) 148–157.

[35] C. Zheng, C. Cao, Z. Ali, In situ formed Bi/BiOBrₓI₁₋ₓ heterojunction of hierarchical microspheres for efficient visible-light photocatalytic activity, Phys. Chem. Chem. Phys. 17 (2015) 13347–13354.

[36] F. Dong, Q. Li, Y. Sun, W.-K. Ho, Noble metal-like behavior of plasmonic bi particles as a cocatalyst deposited on (BiO)₂CO₃ microspheres for efficient visible light photocatalysis, ACS Catal. 4 (2014) 4341–4350.

[37] Y. Sun, Z. Zhao, F. Dong, W. Zhang, Mechanism of visible light photocatalytic NOₓ oxidation with plasmonic Bi cocatalyst-enhanced (BiO)₂CO₃ hierarchical microspheres, Phys. Chem. Chem. Phys. 17 (2015) 10383–10390.

[38] X.A. Dong, W. Zhang, Y. Sun, J. Li, W. Cen, Z. Cui, H. Huang, F. Dong, Visible-light-induced charge transfer pathway and photocatalysis mechanism on Bi semimetal@ defective BiOBr hierarchical microspheres, J. Catal. 357 (2018) 41–50.

[39] J. Safaei, H. Ullah, N.A. Mohamed, M.F. Mohamad Noh, M.F. Soh, A.A. Tahir, N. Ahmad Ludin, M.A. Ibrahim, W.N.R. Wan Isahak, M.A. Mat Teridi, Enhanced photoelectrochemical performance of Z-scheme g-C₃N₄/BiVO₄ photocatalyst, Appl. Catal. B 234 (2018) 296–310.

[40] H. Ullah, A.A. Tahir, T.K. Mallick, Structural and electronic properties of oxygen defective and Se-doped p-type BiVO₄(001) thin film for the applications of photocatalysis, Appl. Catal. B 224 (2018) 895–903.

[41] H. Ullah, A.A. Tahir, S. Bibi, T.K. Mallick, S.Z. Karazhanov, Electronic properties of β-TaON and its surfaces for solar water splitting, Appl. Catal. B 229 (2018) 24–31.

[42] N.A. Mohamed, H. Ullah, J. Safaei, A.F. Ismail, M.F. Mohamad Noh, M.F. Soh, M.A. Ibrahim, N.A. Ludin, M.A. Mat Teridi, Efficient photoelectrochemical performance of γ irradiated g-C₃N₄ and Its g-C₃N₄@BiVO₄ heterojunction for solar water splitting, J. Phys. Chem. C 123 (2019) 9013–9026.

[43] H. Ullah, Inter-molecular interaction in polypyrrole/TiO₂: a DFT study, J. Alloys. Compd. 692 (2017) 140–148.

[44] H. Ullah, A.A. Tahir, T.K. Mallick, Polypyrrole/TiO₂ composites for the application of photocatalysis, Sens. Actuators B Chem. 241 (2017) 1161–1169.

[45] H.S. Park, K.E. Kweon, H. Ye, E. Paek, G.S. Hwang, A.J. Bard, Factors in the metal doping of BiVO₄ for improved photoelectrocatalytic activity as studied by scanning electrochemical microscopy and first-principles density-functional calculation, J. Phys. Chem. C 115 (2011) 17870–17879.

[46] Y. Liu, Y. Zhu, J. Xu, X. Bai, R. Zong, Y. Zhu, Degradation and mineralization mechanism of phenol by BiPO₄ photocatalysis assisted with H₂O₂, Appl. Catal. B 142-143 (2013) 561–567.

[47] E. Mvula, M.N. Schuchmann, C. von Sonntag, Reactions of phenol-OH-adduct radicals. Phenoxyl radical formation by water elimination vs. oxidation by dioxygen, J. Chem. Soc. Perkin Trans. I 2 (2001) 264–268.

[48] D. Vione, V. Maurino, C. Minero, Photosensitised humic-like substances (HULIS) formation processes of atmospheric significance: a review, Environ. Sci. Pollut. Res. Int. 21 (2014) 11614–11622.

[49] K. Min, T. Yum, J. Kim, H.M. Woo, Y. Kim, B.I. Sang, Y.J. Yoo, Y.H. Kim, Y. Um, Perspectives for biocatalytic lignin utilization: cleaving 4-*O*-5 and C*alpha*-C*beta* bonds in dimeric lignin model compounds catalyzed by a promiscuous activity of tyrosinase, Biotechnol. Biofuels 10 (2017) 212.